Towards Development of a Non–Intrusive and Label–Free THz Sensor for Rapid Detection of Aqueous Bio–Samples Using Microfluidic Approach

Nidhi Pandit, *Graduate Student Member, IEEE*, Rahul Kumar Jaiswal, *Graduate Student Member, IEEE*, and Nagendra Prasad Pathak, *Member, IEEE*

***Abstract*—As most of the bio-molecules sizes are comparable to the terahertz (THz) wavelength, this frequency range has spurred great attention for bio-medical and bio-sensing applications. Utilizing such capabilities of THz electromagnetic wave, this paper presents the design and analysis of a new non-intrusive and label-free THz bio-sensor for aqueous bio-samples using the microfluidic approach with real-time monitoring. The proposed THz sensor unit utilizes the highly confined feature of the localized spoof surface plasmon (LSSP) resonator to get high sensitivity for any minute change in the dielectric value near it's surface. The proposed sensor, which is designed at 1 THz, exploits the reflection behavior (S_{11}) of the LSSP resonator as the sensing response. The proposed sensor has been designed with a high-quality factor of *192* to obtain a high sensitivity of *13.5* MHz/mgml^{-1}. To validate the proposed concept, a similar sensor unit has been designed and implemented at microwave frequency owing to the geometry dependent characteristics of the LSSP. The developed sensor has got a highly sensitive response at microwave frequency with a sensitivity of *1.2771e-4* MHz/mgml^{-1}. A customized read-out circuitry is also designed and developed to get the sensor response in terms of DC-voltage and to provide a proof of concept for the low-cost point of care (PoC) detection solution using the proposed sensor. It is anticipated that the proposed design of highly sensitive sensor will pave a path to develop lab-on-chip systems for bio-sensing applications.**

***Index Terms*—Bio-sensing, label-free, localized spoof surface plasmon (LSSP), non-intrusive, terahertz.**

I. Introduction

DUE TO THE vital role of the life sciences and medical therapeutic, there is always being a great surge for bio-sensing in biotechnology research. The main goal of the bio-sensing is to spot the bio-molecules and their interactions. Especially since the last decade, a lot of research has been carried out in this domain for the accurate detection of the bio-molecule [1]–[6]. Traditional electrochemical and optical technologies have labeled detection [1]–[2]. Recently, the label-free bio-sensing approach [3] has got great attention and has become an emerging research domain due to the contamination of the samples and complex procedure of the labeled detection.

Terahertz (THz) frequency band lies in between the microwave and far-infrared of the EM spectrum. As THz waves are non-ionizing and their wavelengths are comparable to the size of most of the bio-molecules [4], [5], it makes them effective in developing highly sensitive, label-free, and non-intrusive sensors. However, THz waves for sensing are mainly limited for the dry sample specimen because the aqueous samples are very lossy and absorb the EM waves because of the heavy water content in the samples [6].

In order to utilize the exotic properties of the THz EM waves for the detection of the biomolecules in the aqueous sample, a different technique needs to be adopted rather than a conventional one. The techniques must enhance the EM wave-matter interaction and control the water absorption in order to provide an improved sensing response. This interaction can be improved by confining and localizing the EM field in the sub-wavelength region so that a small amount of the aqueous sample can be used to detect the analytes. This EM wave confinement and localization can be achieved by systematic manipulation of the EM wave by slowing down its velocity. Many approaches have been provided in the literature to manipulate the EM field, among which the metamaterial approach has gained a lot of attention [7]–[13]. One of the effective and systematic manipulations of the EM wave is achieved by using the controllable dispersive properties of the spoof surface plasmon polaritons (SSPP). SSPP's are the lower frequency counterpart of the optical SPP modes [11]–[13], which are the highly confined and localized modes at the interface of the metal and dielectric where dielectric permittivity changes its sign across the interface. These confined EM fields are used to develop sensors at optical frequency. However, these features are not supported at THz and microwave frequency regimes because the wave penetration is much smaller than the wavelength of the incoming EM wave, which reduces the EM confinement. To achieve the highly confined modes at these lower frequency regimes, periodic corrugations have been made on the metallic surface by perforating the surface with grooves or holes to allow the EM wave to effectively penetrate the corrugated surface [14]–[16]. These corrugations reduce the group and phase velocities of the EM waves. Hence, such type of mode is called as the spoof or designer surface plasmon polaritons. It is reported that the closed corrugated geometries

Manuscript received September 8, 2020; revised December 14, 2020; accepted January 7, 2021. Date of publication January 12, 2021; date of current version March 30, 2021. *(Corresponding author: Nagendra Prasad Pathak.)*

The authors are with the Department of Electronics and Communication Engineering, Indian Institute of Technology Roorkee, 247667 Roorkee, India (e-mail: npandit@ec.iitr.ac.in; rjaiswal@ec.iitr.ac.in; nagendra.pathak@ece.iitr.ac.in).

Color versions of one or more figures in this article are available at https://doi.org/10.1109/TBCAS.2021.3050844.

Digital Object Identifier 10.1109/TBCAS.2021.3050844

also support these confined modes and are called as localized spoof surface plasmons (LSSP) [12], [13]. Thus, the corrugated metallic surfaces are able to support highly confined modes near the grooves part and allow their propagation properties to be controlled by its geometrical parameters. Exploiting the properties of the SSPP, many of the work related to the transmission line and other components at THz and microwave frequency has been reported in [14]–[18].

To reduce the absorption of the THz waves through aqueous samples along with confining the EM waves, one should look for a solution to reduce the sample size. In this direction, microfluidic approach has emerged as an effective tool to hold the small sample sizes. To design the microfluidic channel, a low-cost and flexible Polydimethylsiloxane (PDMS) material is found to be an attractive choice to the sensor designer due to its optically transparent and chemically inert nature [19]–[21].

Thus, combining both features of the high EM field confinement of the LSSP based sensor and microfluidic approach has opened a new vista to develop highly sensitive sensors for aqueous bio-samples. The presented work focuses on the design and development of the low-cost, low-profile, and easy to fabricate planar sensors for the detection of the analyte in aqueous biological samples both at THz as well as at microwave frequency. Here, blood plasma with different concentrations of glucose has been considered as biological SUTs. Based on the above discussion, the proposed work has been organized in the following sections and are as follows: Section II deals with the theoretical background and the operational principle of the sensor. Then in Section III, a sensing unit has been designed at THz frequency, which utilizes a corrugated LSSP ring-resonator and provides an enhanced EM wave confinement on its surface. Further, EM analysis of the sensor along with the microfluidic channel and aqueous SUTs has been presented at THz frequency. For the experimental validation of the proposed approach, a similar structure has been designed and fabricated at microwave frequency, which is provided in Section IV. Section V presents a customized read-out circuitry to provide the proof of the concept for its feasibility as a point of care applications. Finally, Section VI discusses the results findings and future scope of the presented work.

II. Theoretical Background

A. Cole-Cole Model for Polar Liquids

The complex permittivity of any material defines its behavior with respect to the EM field. When any polar liquid is exposed in an EM field, their molecular dipoles start to rotate as shown in Fig. 1. This rotation leads to an energy loss that is associated with the intermolecular friction and an increase in the stored energy associated with the polarization of the molecules [22]. The complex permittivity of the polar liquid can then be written as $\varepsilon = \varepsilon_1\text{-}j\varepsilon_2$, where real ($\varepsilon_1$) and imaginary ($\varepsilon_2$) parts of the ε are well described by the Cole-Cole model as follows (1) and (2).

$$\varepsilon(\omega,\chi) = \varepsilon_1(\omega,\chi) - j\varepsilon_2(\omega,\chi) = \varepsilon_\infty(\chi) + \frac{\Delta\varepsilon(\chi)}{1+(j\omega\tau(\chi))^\alpha} \quad (1)$$

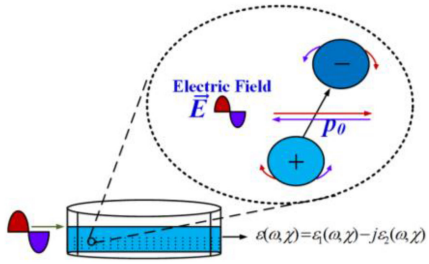

Fig. 1. Illustration of the polarization in polar molecules in the presence of an alternating electric field.

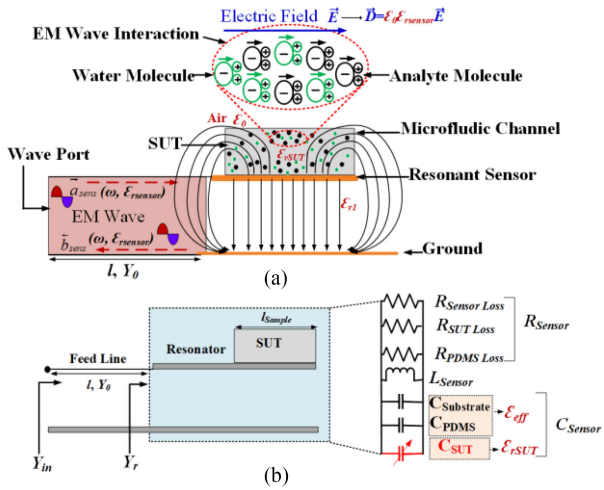

Fig. 2. Illustration of (a) Sensing mechanism and (b) Corresponding lumped electrical equivalent circuit of the proposed ring resonator sensor.

Here, for $\alpha = 1$ (for single pole),

$$\varepsilon_1(\omega,\chi) = \varepsilon_\infty(\chi) + \frac{\Delta\varepsilon(\chi)}{1+\omega^2\tau^2}, \varepsilon_2(\omega,\chi) = \frac{\Delta\varepsilon(\chi)\cdot\omega\tau}{1+\omega^2\tau^2} \quad (2)$$

with $\Delta\varepsilon(\chi) = \varepsilon_\infty(\chi) - \varepsilon_s(\chi)$ ε_s and ε_∞ are the permittivity in the static and high-frequency range, respectively. τ is the relaxation time, and α is the distributed parameter in each dielectric dispersion and signifies the number of poles.

B. Sensing Mechanism

Fig. 2 illustrates the concept of the proposed work along with its corresponding equivalent electrical circuit model. The proposed work is capable of evaluating any polar analyte characteristics in an aqueous medium using its behavior with respect to the high-frequency EM field. According to (1)–(2), the dielectric behavior of the sample under test (SUT) changes according to the concentration of the analyte and, consequently, the SUT response with respect to the high-frequency EM-field.

As aqueous SUT contains a large percentage of water in it, which is also polar in nature, the overall dielectric constant of the SUT, $\varepsilon_{rSUT,}$ mainly depends upon the dielectric constants of both the base ε_{rB} and analyte, ε_{rA}, and fractional volume of analyte in the base f_{vol}, respectively and governed by

the Maxwell-Garnet mixture theory [23]. For diluted mixture ($f_{vol}<<1$), according to this theory, $\varepsilon_{rSUT,}$ is given by (3);

$$\varepsilon_{rSUT}(\omega,\chi) = \varepsilon_{rB}(\omega,\chi) + 3\cdot\varepsilon_{rB}(\omega,\chi) f_{vol}\frac{(\varepsilon_{rA}(\omega,\chi)-\varepsilon_{rB}(\omega,\chi))}{(\varepsilon_{rA}(\omega,\chi)+2\cdot\varepsilon_{rB}(\omega,\chi))} \quad (3)$$

The overall permittivity of the sensor ($\varepsilon_{rsensor}$) including microfluidic channel and SUT can be expressed as (4);

$$\varepsilon_{rsensor}(\omega,\chi) = \varepsilon_{eff} + \alpha[\varepsilon_{rSUT}(\omega,\chi) - \varepsilon_{air}] \quad (4)$$

Where ε_{rSUT} and ε_{air} are dielectric constants of the SUT and air, respectively, and α is a coefficient related to the sensor's sensitivity. ε_{eff} is the unloaded effective dielectric constant of the sensor in presence of the microfluidic channel.

In presence of SUT, the capacitance of the sensor C_{sensor}, can be expressed in terms of the relative permittivity $\varepsilon_{r\text{sensor}}$ (= $\varepsilon_{sensor}/\varepsilon_0$) and capacitance in presence of the air, i.e., C_0 as given in (5);

$$C_{sensor}(\omega,\chi) = \varepsilon_{rsensor}(\omega,\chi)\cdot C_0 \quad (5)$$

A change in the permittivity of the resonant sensor ($\Delta\varepsilon_{rsensor}$) with respect to the change in the concentration of the analyte ($\Delta\chi$), as discussed in (4), will also change the reflected EM wave due to the change in the input impedance and so the complex reflection coefficient as given in (6);

$$\Gamma(\omega,\varepsilon_{rsensor}) = \frac{\vec{b}_1(\omega,\varepsilon_{rsensor})}{\vec{a}_1(\omega,\varepsilon_{rsensor})} = \frac{Y_{in}-Y_0}{Y_{in}+Y_0} \quad (6)$$

Where $\vec{a}_1(\omega,\varepsilon_{rsensor})$: incident EM wave; $\vec{b}_1(\omega,\varepsilon_{sensor})$: reflected wave; ω: angular frequency of operation; χ: concentration of the analyte, Y_0: characterstics admittance, and Y_{in}:input admittance of sensing unit.

For one port, return loss, S_{11} is equal to Γ and written as (7);

$$S_{11} = \Gamma(\omega,\varepsilon_{rsensor}) = \frac{Y_{in}-Y_0}{Y_{in}+Y_0} \quad (7)$$

The input admittance of the sensor Y_{in} can be deduced as;

$$Y_{in} = Y_0\frac{Y_r + jY_0\tan\beta l}{Y_0 + jY_r\tan\beta l} \quad (8)$$

With

$$Y_r = G_{sensor} - j/\omega L_{sensor}(\omega) + j\omega C_{sensor}(\omega,\chi) \quad (9)$$

Where R_{sensor} $(=1/G_{sensor}) = R_{PDMS\ Loss} + R_{SUT\ Loss} + R_{sensor\ Loss}$, L_{sensor}, and $C_{sensor} = C_{substrate} + C_{PDMS} + C_{SUT}$, are the total resistance, inductance, and capacitance of the loaded resonator, respectively. By putting the values of (8) and (9) into (7) results into (10);

$$S_{11} = A\cdot\left[\frac{(G_{sensor}-j/\omega L_{sensor}(\omega)+j\omega C_{sensor}(\omega,\chi))-Y_0}{(G_{sensor}-j/\omega L_{sensor}(\omega)+j\omega C_{sensor}(\omega,\chi))+Y_0}\right]$$
$$\text{where}: A = (1-j\tan\beta l)/(1+j\tan\beta l), \text{and}$$
$$C_{sensor}(\omega,\chi) = C_0\cdot\{\varepsilon_{eff} + \alpha[\varepsilon_{rSUT}(\omega,\chi) - \varepsilon_{air}]\} \quad (10)$$

S_{11} is a complex quantity and expressed in terms of magnitude and phase, i.e., $S_{11} = |S_{11}|e^{+j\phi}$. The phase ϕ of the sensor mainly consists of two components: (i) phase of the input transmission line (ϕ_l), and (ii) phase of the resonator (ϕ_r). The ϕ_r is related to the permittivity $\varepsilon_{rsensor}$ and sample length, l_{sample} through the phase vector β as (11);

$$\varphi_r = \beta l_{sample} = \frac{2\pi\sqrt{\varepsilon_{rsensor}(\omega,\chi)}}{\lambda_0}\cdot l_{sample} \quad (11)$$

Here, λ_0 is the free-space wavelength. The corresponding frequency behavior of the resonator can be obtained from (12).

$$f_{\text{Response}} = \frac{d}{dt}(\varphi_r) = \frac{d}{dt}(\beta l_{sample})$$
$$= \frac{d}{dt}\left[\frac{2\pi\sqrt{\varepsilon_{rsensor}(\omega,\chi)}}{\lambda_0}.l_{sample}\right] \quad (12)$$

The magnitude of the S_{11}, i.e., $|S_{11}|$ in dB can be given as (13) shown at the bottom of this page.

From (10)–(13), it is understood that any change in the analyte concentration χ will be translated into the magnitude, phase and frequency behavior of S_{11} parameter of the resonant sensor.

C. Sensitivity and Perturbation Theory

Based on the E-field distribution on the sensor, the sensing mechanism is often described by the perturbation theory. It states that when a polar SUT is placed in the high E-field region of the sensor, it perturbs the stored energy and dielectric loss of the resonant device due to the change in the polarization and loss factor of the analyte in the SUT. This perturbation can be seen in terms of the change in the resonant frequency and Q-factor, respectively and expressed as (14);

$$\frac{f_{loaded} - f_{unloaded}}{f_{loaded}}$$
$$= \left(\frac{\varepsilon_0 - \varepsilon_{sensor}}{2\varepsilon_0}\right)\frac{\iiint_{V_s} E^*_{unloaded}\cdot E_{loaded}dV}{\iiint_{V_c}|E_{unloaded}|^2 dV} \quad (14)$$

Where V_s and V_c represent the sample and cavity volumes, respectively. Whereas f_{loaded} and ε_{sensor} represent the resonating frequency and complex permittivity of the sensor in loaded

$$|S_{11}|\,(dB) = 20\log_{10}$$
$$\left|A\cdot\left[\frac{(G_{sensor}-j/\omega L_{sensor}(\omega)+j\omega C_{sensor}(\omega,\chi))-Y_0}{(G_{sensor}-j/\omega L_{sensor}(\omega)+j\omega C_{sensor}(\omega,\chi))+Y_0}\right]\right|$$
$$\text{where}: A = (1-j\tan\beta l)/(1+j\tan\beta l), \text{and}$$
$$C_{sensor}(\omega,\chi) = C_0\cdot\{\varepsilon_{eff} + \alpha[\varepsilon_{rSUT}(\omega,\chi) - \varepsilon_{air}]\} \quad (13)$$

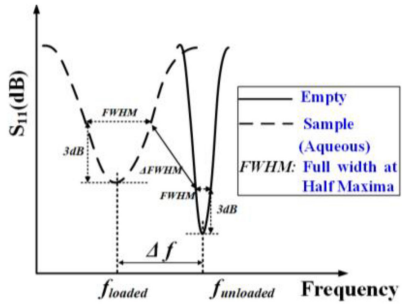

Fig. 3. Typical response of reflection of the one-port parallel resonator with and without sample (in this case, a liquid).

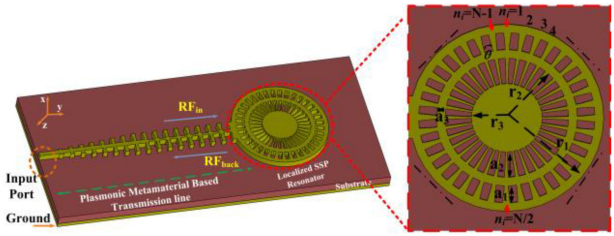

Fig. 4. Layout of the proposed sensor.

condition, respectively. Similarly, $f_{unloaded}$ and ε_0 represent the resonance frequency and permittivity for free-space, respectively. $E_{unloaded}$ and E_{loaded} are the E-fields of the empty and loaded conditions, respectively.

Sensitivity (S) is one of the main performance parameters of the sensor and defined as the change in the electrical behavior (viz. resonating frequency, i.e., Δf_{sensor} or Q-factor, i.e., ΔQ) with respect to the change in the dielectric constant $\Delta\varepsilon_{SUT}$ or the concentration of the analyte $\Delta\chi$ and expressed as (15);

$$S = \frac{\Delta f_{sensor}}{\Delta\varepsilon_{SUT}} or \frac{\Delta f_{sensor}}{\Delta\chi} \tag{15}$$

This is also visible from Fig. 3, which depicts the sensor response for the one-port sensor in terms of change in the electric behavior of the sensor in the presence of the SUT.

After analyzing (1)–(15), it is found out that the following analysis needs to be done to ensure the maximum sensitivity, which is summarizes as;

1) To get the high E-field–SUT interaction, EM wave must confine and localize at the sensor surface. To ensure this its phase and group, velocities need to be slowed down.
2) The sensor should have High–Q factor($= f/FWHM$).
3) The maximum EM wave and matter interaction takes place near the high E-field regions (hot-spot) so the hot-spot region needs to be specified to place the SUT.

III. Design and Simulation of THz Sensor

Based on the above discussion, this section proposes the design of the highly sensitive sensor by exploiting the properties of the LSSP at THz frequency using a microfluidic approach. The layout of the proposed sensor has been shown in Fig. 4.

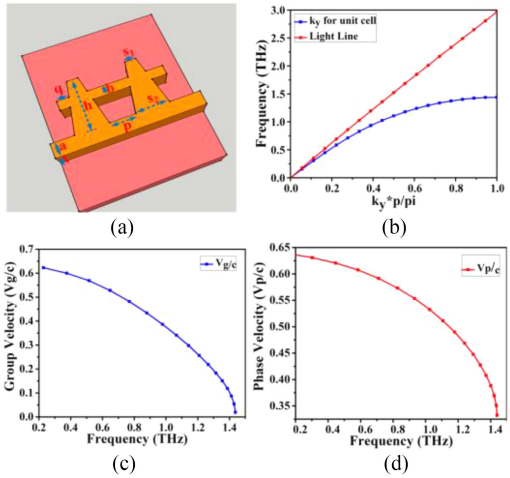

Fig. 5. (a) Unit cell of sensor ring, and its (b) Dispersion curve, (c) Group velocity, (d) Phase velocity analysis.

This sensing unit consists of a LSSP resonator, which has been fed by the SSPP transmission line at its input port. This LSSP resonator is realized by using the closed geometry of the periodic corrugations. It has been designed on both side metalized dielectric substrate with a dielectric constant of *2.2*, a loss tangent of 0.0009, and a height of 20 μm. The copper metal of thickness *0.35* μm is used as the metallization. The proposed ring has $r_1 = 20\,\mu$m, $r_2 = 14\,\mu$m, $r_3 = 8\,\mu$m, and mean periphery $(2\pi r) = 110\,\mu$m with number of grooves $N = 72$. The lattice constant of the unit cell (p) in the ring resonator is calculated according to $l/N = 2\pi r/N$. The beauty of this closed LSSP ring resonator is that its electromagnetic properties, viz. dispersion, cut-off frequency, phase, and group velocities, can be controlled through its structural parameters. A unit cell of the periodic corrugation has been analyzed to study these properties and is shown in Fig. 5. Fig. 5(a) shows the layout of the unit cell along with the geometrical parameters. The geometrical parameter values of the unit cell used in proposed sensing resonator are given as follows (all are in μm): $a = 56$, $b = 10$, $t = 0.35$, $p = 6.675$, $q = 10.835$, $h = 80$, $s_1 = 2$, $s_2 = 5$.

The operating frequency, and hence the structural parameters of the sensor have been chosen considering the relaxation frequency of water because aqueous bio-samples are mainly composed of water. The unit cell of the textured ring resonator of the proposed sensor has been shown in Fig. 5(a). The dispersion of this unit cell has been analyzed using Eigenmode solver of the CST Microwave Studio and presented in Fig. 5 (b). Here, red and blue colored curves show the dispersion curve for the freely propagating wave (k_0) and LSSP unit cell (k_y), respectively. It is observed that at lower frequency, k_y is similar to k_0, however, as frequency increases and approaches to the cut off frequency, the k_y becomes much larger than the k_0.

In other words, near the cut-off frequency, the group and phase velocities decrease with an increase in k_y, as shown in Fig. 5 (c) and (d), respectively, since k_y is directly related to the phase and group velocities by these relations $v_p = \omega/k_y$ and $v_g = d\omega/dk_y$. This indicates the EM wave is slowed down, and

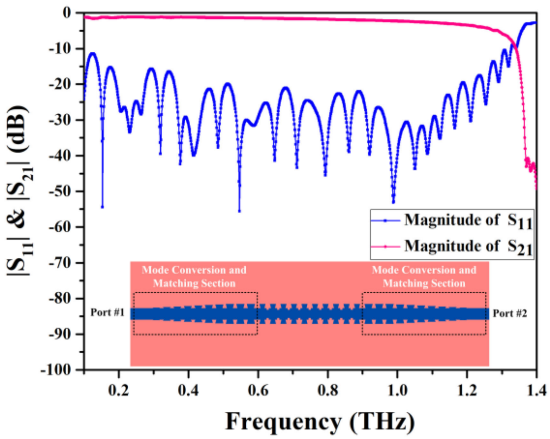

Fig. 6. Simulated S-parameter response back to back transition used to feed the resonator (Inset: layout of transition).

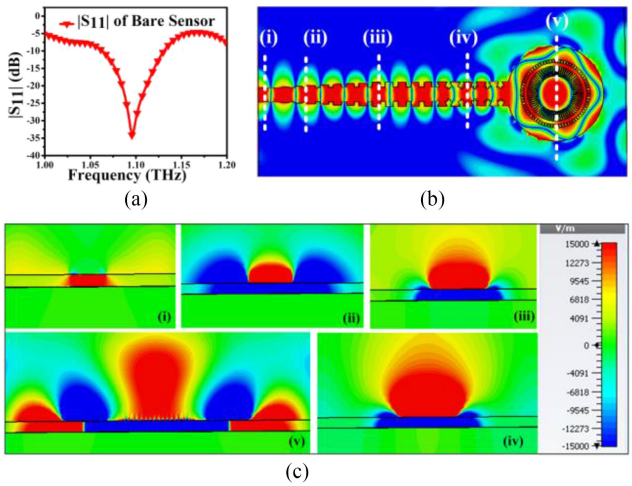

Fig. 7. (a) S-parameter, (b) Corresponding complete electric field distribution of structure, and (c) Normal electric field at different locations of the sensor.

thus sub-wavelength confinement and localization of the EM field are obtained using the LSSP concept, which in turn results in an enhancement of the EM wave-matter interaction at the sensor unit. However, this LSSP resonator needs to be excited efficiently. In order to efficiently excite the designed resonating unit, an SSPP transmission line has been utilized that consist of a mode converter section to convert the QTEM mode of the microstrip to the TM mode of the LSSP ring resonator. The full-wave EM simulation results of the designed SSPP transmission line have been provided in Fig. 6 in terms of S-parameter, which indicates the efficient transmission performance of the SSPP transmission line. Fig. 7(a) depicts the S-parameter response of the proposed LSSP sensor (bare) at THz frequency, which shows the resonance of the LSSP ring resonator at 1 THz. The operating frequency and the structural parameters of the proposed sensor have been chosen considering the relaxation frequency of water due to the fact that aqueous bio-samples are mainly composed of water. The phase change ($\Delta\phi$) of the surface mode with a wavelength λ_{res} in the ring resonator of

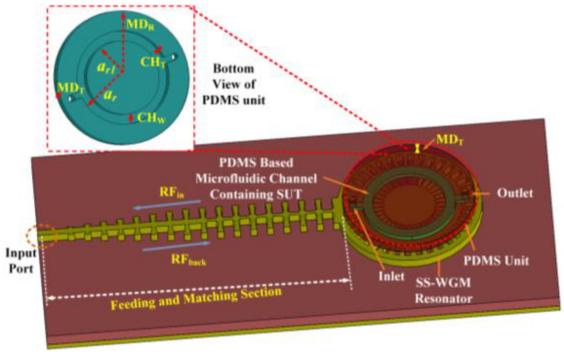

Fig. 8. EM simulation model of the proposed sensor in the presence of SUT and PDMS enabled microfluidic channel.

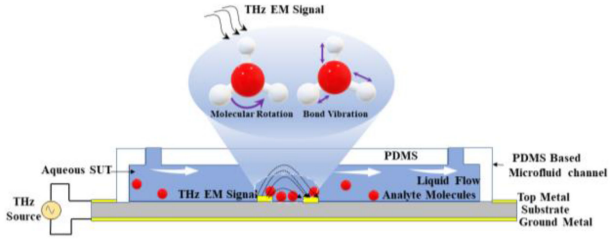

Fig. 9. EM simulation model of the proposed sensor in the presence of SUT and PDMS enabled microfluidic channel.

radius r, and effective dielectric constant ε_{eff} is given by $\Delta\phi = 4\pi^2\sqrt{\varepsilon_{eff}}.r/\lambda_{res}$. The resonance is achieved when the $\Delta\phi$ becomes the integral multiple of π, indicating the minimum reflection at port one. The sensor has been designed to achieve a High–Q factor (low full width at half maxima: FWHM) of 192 that corresponds to a high-resolution capability of the sensor for detecting the analyte in SUT. The optimized physical dimensions of LSSP resonator are as follows (all are in μm): $a_1 = 3.98$, $a_2 = 5.99$, $a_3 = 2$, $r_1 = 20$, $r_2 = 14$, $r_3 = 8$; and $N = 72$, $\theta = 10^o$.

To get a better insight into the EM field localization and confinement, the normal component of the E-field on the proposed sensor has been calculated at different locations (i)-(v) of Fig. 7(b) and illustrated in Fig. 7 (c). It is observed that the E-field is negligible initially (at the location (i)). However, as one moves further towards the resonating element, the E-field is enhancing, and becomes maximum at the LSSP based resonating element.

Fig. 8 illustrates the EM simulation setup for the proposed sensor. The PDMS based microfluidic channel along with SUT on the sensor have been simulated for different concentrations of the analyte. This microfluidic channel is made up of the PDMS material having dielectric constant and loss tangent of *2.5* and *0.05,* respectively [24]. In Fig. 8 and Fig. 9, the microfluidic channel has outer radius: a_r, inner radius a_{r1}, channel width CH_W, channel thickness CH_T. The PDMS mould has radius MD_R and thickness MD_T.

To analyze the performance of the complete sensing system, as shown in Fig. 8, with different concentrations of analyte, it is modelled in CST microwave studio and simulated using a time-domain solver that is based on the finite integration

TABLE I
COLE-COLE MODEL FOR AQUEOUS GLUCOSE AT THZ FREQUENCY

S. No.	Concentration		Cole-Cole Model Parameter For Aqueous Glucose [25]			
	$(mol\ L^{-1})$	$(mg\ ml^{-1})$	ε_s	ε_∞	τ	α
1.	0 (Only Water)	0	78.5	2.5	9.5	1
2.	0.9	162.14	70.6	5.6	12.6	0.9
3.	1.5	270.23	60.0	2.49	9.5	1
4.	4.7	846.73	34.3	2.5	9.5	1

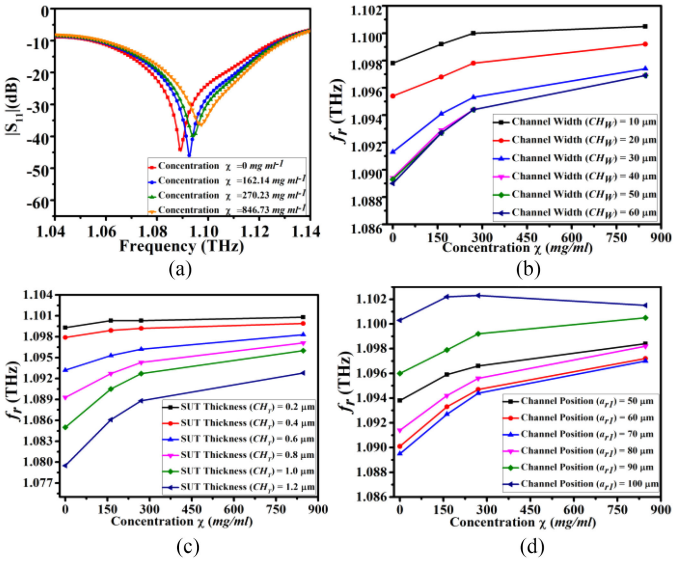

Fig. 10. (a) Initial S-parameter simulation of the proposed sensor with different glucose concentration and sensor response for (b) Different sample thickness (CH_T) while keeping other parameters constant, (c) Different channel position (a_{r1}) while keeping other parameters constant, (d) Different channel width (CH_W) while keeping other parameters constant.

technique (FIT). For a given frequency range, number of frequency points, and appropriate boundary conditions, it divides the structure into the small mesh cells and solve them. The final response, in terms of S-parameters, is obtained by integrating the responses of all small mesh cells. In the simulator, SUT inside the microfluidic channel has been modeled as a material using the parameters given by the experimental single-pole Cole-Cole model for different concentrations of glucose as reported in [25] and given in Table I.

When the THz frequency signal interacts with the SUT in the microfluidic channel, as shown in Fig. 9, it stimulates the molecular rotation and/or vibration in the molecular bonds. This process results into the storage of energy due to the polar movement of molecules and some losses due to the molecular friction. According to the Cole-Cole theory, as discussed above, this additional stored energy and losses corresponding to the individual concentration of the analytes can be translated in terms of their complex dielectric permittivity. This change in the dielectric permittivity of each concentration of glucose (analyte) can be seen in the S-parameter signature of the proposed sensing device. It can be verified from Fig. 10(a), which signifies that as the concentration of the glucose changes, a blue shift of the

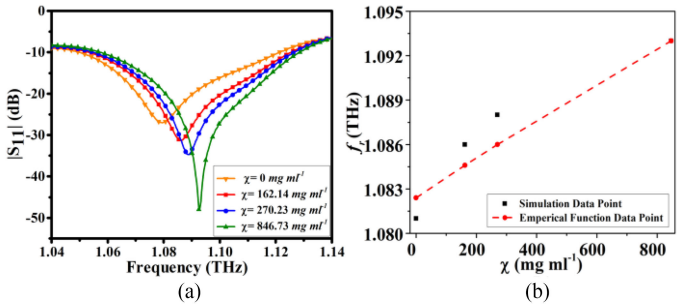

Fig. 11. (a) One port S-parameter results with different concentration of the glucose in SUT at THz, and corresponding (b) Resonating frequency with respect to different concentrations of glucose.

resonant frequency is observed. Similarly, for the concentrations of glucose where the stored energy is greater than losses due to friction, it enhances the matching of the sensor, and thus there is an increase in the value of $|S_{11}|$ dB. Whereas, for concentrations, where losses due to the friction are more prominent, it reduces the Q-factor as well as $|S_{11}|$ (dB).

In order to ensure the maximum sensitivity of the proposed sensor, the channel volume and channel position needs to be optimized. A comprehensive analysis is performed for that as shown in Fig. 10(b)–(d). Fig. 10(b) depicts the analysis of the sensor with respect to the channel width (CH_W) variation while keeping other parameters constant, and it is observed that sensitivity of the sensor increases first with an increase in the CH_W; however, after a particular CH_W, the sensitivity becomes almost constant and no variation in the sensitivity is observed with respect to the change in the CH_W. Further, it has been noticed from Fig. 10(c) that as the SUT thickness (CH_T) increases while keeping other parameters constant, the sensitivity of the sensor increases. Fig. 10(d) illustrates that by moving the channel position (a_{r1}) away from the center while keeping other parameters constant, sensitivity increases first and then decreases after a particular value of a_{r1}.

Based on the above-detailed analysis, the optimum parameters of the channel position (a_{r1}), channel width (CH_W), sample thickness (CH_T) and other physical dimensions of the microfluidic channel containing PDMS unit have been chosen to obtain maximum sensitivity of the sensor and are as follows (all are in μm): $a_r = 110$, $a_{r1} = 70$, $CH_T = 1$, $CH_W = 40$, $MD_R = 115$, $MD_T = 1.2$. Fig 11(a) presents the sensor response in terms of $|S_{11}|$ with the optimized parameters. Correspondingly, Fig. 11(b) plots the resonant frequency, f_r, as a function of glucose concentration, χ. Based on the analysis, the mathematical relationship between the resonant frequency and the concentration of the analyte can be given as (16);

$$f_r = 1.35e - 5 \cdot \chi + 1.0824 \tag{16}$$

As the sensitivity (S) and limit of detection (LOD) are the main performance parameters of any sensor, they are also discussed here. The S is defined as the change in the resonating frequency of the sensor, i.e., Δf_r with respect to change in the concentration of the analyte $\Delta\chi$ and given as $S = \Delta f_r / \Delta\chi$. S is found to be 13.5 MHz/mgml^{-1} for the proposed sensor. Similarly, LOD is

TABLE II
PERFORMANCE PARAMETER OF THE SENSOR

Performance Parameter	Relation/Value
Empirical Expression	$f_r = 1.35e-5 \cdot \chi + 1.0824$
R^2 value	0.95
Sensitivity (S)	13.5 MHz/mgml^{-1}
Resolution	22.2 mg/ml

*S: Frequency sensitivity, R^2: Confidence value

defined as the minimum amount of the analyte concentration that can be detected through the sensor also known as resolution and given as $LOD = f_{resol.}/S$ [26], where f_{resol} is the resolution and calculated as $f_{resol} = F_{Smax}$-$F_{Smin}/(n_p$-$1)$. Here, F_{Smax} and F_{Smin} are the maximum and minimum frequencies of the observation window, and n_p is the number of frequency points in this range of frequency. To find the *LOD*, an EM simulation has been performed in the range of 0.9 THz to 1.2 THz with 1001 frequency points. Correspondingly, the resolution, i.e., *LOD* value of the proposed sensor, is found to be 22.2 mg/ml at THz frequency regime. Further, corresponding performance parameters, including empirical expression of the sensor, have been provided in Table II, which shows that the proposed sensor has improved performance in terms of the sensitivity and compatibility of integration with planar ICs.

IV. EXPERIMENTAL VALIDATION AT MICROWAVE FREQUENCY

Due to the non-availability of the THz fabrication and characterization facilities, similar sensor has been redesigned at microwave frequency, thanks to the geometrical parameters dependence of the LSSP. All the parameters of the LSSP sensor unit and microfluidic channel have been scaled up as it was at THz frequency for the design at microwave frequency. The sample preparation of SUT, along with the fabrication of the sensor and microfluidic channel, are discussed below.

A. Sample Preparation

To validate the sensor performance, organic bio-sample, i.e., blood plasma with different concentrations of glucose, have been prepared as SUTs. The samples have been prepared with D-glucose, bovine serum albumin (BSA), plasma serum (all are from HiMedia laboratories), and distilled water. This plasma serum does not contain any WBC (white blood cell) and RBC (red blood cell) as it is extracted from the blood after coagulation and optically transparent in nature. A sample stock having a concentration of m = Y/X g/ml has been prepared via Y g of glucose and X ml of distilled water. This solution was then sterilized by autoclaving at 121°C at 15 psi for 20 minutes. After that, this stock media is mixed with Y mg of BSA and Y/10 ml of plasma serum in a contamination-free medium (in a laminar). For example, 0.5 g/ml glucose sample stock is prepared with 10 g of D-glucose, 20 ml of distilled water, 10 mg of BSA, and 1 ml of plasma serum. From the prepared sample stock, a lower concentration of samples has been prepared by diluting it with distilled water according to the volumetric conversion (17); where N_{stock} and V_{stock} are the concentration and volume of the sample stock, while N_{SUT} and V_{SUT} are the concentrations and volume of SUT, respectively.

$$N_{stock}V_{stock} = N_{SUT}V_{SUT} \tag{17}$$

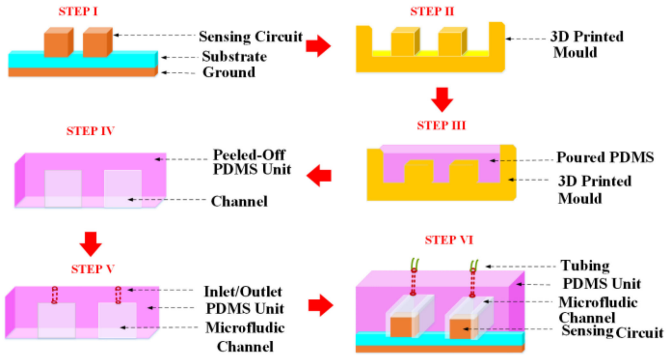

Fig. 12. Side view of step-by-step fabrication process of 3D printed PDMS microfluidic channel mould.

B. Sensor and Microfluidic Channel Fabrication

Fig. 12 depicts the step-by-step procedure to develop the microfluidic channel. Step I begins with the determination of the dimensions of the 3D reusable mould according to the sensor hot-spot footprint. In Step II, this mould has been designed using 3D CAD tool and developed using an in-house printing facility "Projet MJP 3600" in a layer by layer formation. Then the fabricated mould has been cleaned properly with isopropyl alcohol and highly pressurized hot water to completely wipe out the wax and other adhered chemicals involved in the 3D printing process. In Step III, the liquid Sylgard-184 PDMS (Polydimethylsiloxane) resin is mixed with its curing agent in 10:1 weight ratio to convert the liquid PDMS into solid and then thoroughly stirred for at least 10 minutes to assure proper mixing before pouring into 3D reusable mould. After that, the 3D mould along with PDMS resin, had been kept in a degassing unit for two hours to remove all the air bubbles from the PDMS resin. Once all the air bubble comes out from the mixture, it is kept into the hot air oven with 80°C for two hours. Then in Step IV, this cured PDMS mould, which contains micro-channels in it, had been peeled off very carefully from 3D mould. To infuse the SUT and to collect waste from the micro-channels, inlet and outlet holes have been made with the help of 1 mm biopsy punch as shown in Step V. Finally, prepared microfluidic channel along with the tubing has been placed above the sensing hot-spot region as shown in Step VI.

The proposed sensor has been designed at microwave frequency on a Neltec substrate with a dielectric thickness of 3.38, loss tangent of *0.0024,* and a height of 1.52 mm covered with a copper cladding of 35 μm. The propagation properties of the designed unit cell, as shown in Fig. 5(a), at microwave frequency have been analyzed, and corresponding dispersion and group velocity have been provided in Fig. 13(a) and (b), respectively. This verifies the similar characteristic behavior at microwave frequency. The proposed sensor and PDMS unit, as shown in Fig. 13 (c), have been fabricated with optimized

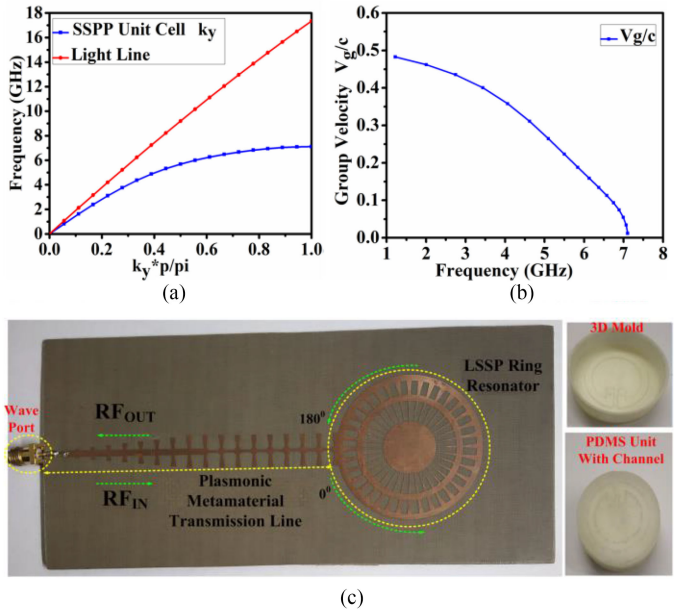

Fig. 13. (a) Dispersion curve, (b) Normalized group velocity of unit cell of the proposed sensor unit at microwave frequency, (c) Fabricated prototype of the sensor, printed 3D reusable mould, and microfluidic PDMS unit.

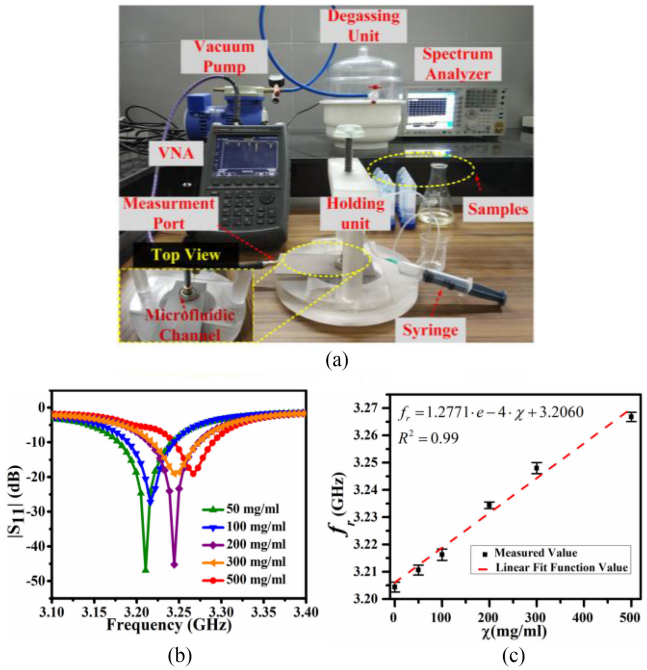

Fig. 14. (a) Experimental setup at microwave frequency for characterizing the proposed sensor, with corresponding (b) One port S-parameter with different concentrations of glucose in SUT, and (c) Resonating frequency with respect to different concentration of glucose.

physical parameters, which are as follows (all are in mm): $a = 2$, $b = 2$, $t = 0.35$, $p = 1.63$, $q = 0.32$, $h = 12$, $s_1 = 0.40$, $s_2 = 1.70$, $a_1 = 3.98$, $a_2 = 5.99$, $a_3 = 2$, $r_1 = 20$, $r_2 = 14$, $r_3 = 8$, $a_r = 12$, $a_{r1} = 15$, $CH_T = 0.4$, $CH_W = 3$, $MD_R = 20$, $MD_T = 10$; and $N = 36$, $\theta = 10^o$. Standard chemical

TABLE III
PERFORMANCE PARAMETER OF THE SENSOR

Performance Parameter	Relation/Value
Empirical Expression	$f_r = 1.2771e-4 \cdot \chi + 3.2060$
R^2 value	0.99
Sensitivity (S)	1.2771e-4 MHz/mgml^{-1}
Resolution	73.3 mg/ml

*S: Frequency sensitivity, R^2: Confidence value

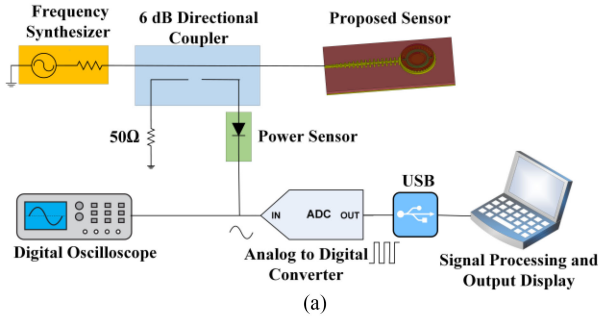

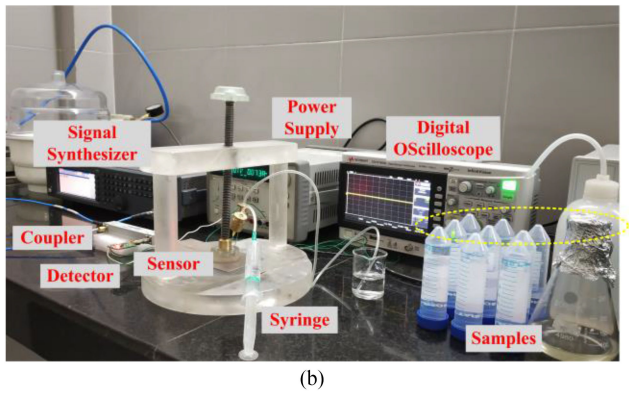

Fig. 15. (a) Schematic description, and (b) Experimental setup of sensing device with customized readout circuitry.

TABLE IV
OUTPUT VOLTAGE OF CUSTOMIZED READOUT CIRCUITRY

S. No.	Concentration (mgml^{-1})	Incident Input Power (dBm)	Average Output Voltage (mV)
1.	Bare	-10	990
2.	0	-10	845
3.	100	-10	830
4.	200	-10	808
5.	300	-10	795
6.	500	-10	776

photolithography and wet etching technique have been used for the fabrication.

C. Experimental Setup

Fig. 14.(a) depicts the experimental arrangement for the characterization of the proposed sensor performance with the SUTs having different glucose concentrations at microwave frequency. To get maximum sensitivity, the microfluidic channel has been aligned precisely over the sensor hot-spot. An in-house developed fixing unit has been used to align and fix the microfluidic channel above the sensor and to avoid any kind of leakage.

TABLE V
COMPARISON OF THE PROPOSED SENSOR WITH THE STATE OF THE ART

Ref.	Linear Concentration Range	Maximum Sensitivity	Resolution	Intrusive/ Non-intrusive	Detection	Life Span
[28]	0–3000 μM	27.2 mA $mM^{-1}cm^{-2}$	87.9 μM	Intrusive	Label-Free	Limited
[29]	0.4–4 μM	89.035 μA mM^{-1}	-	Intrusive	Label-Free	Limited
[30]	0–70 μM	6.90 nA μM^{-1}	-	Non-Intrusive	Label-Free	Not limited
[31]	0.7–1.2 mg/ml	6.2 dB/mg ml^{-1}	-	Non-Intrusive	Label-Free	Not limited
[32]	4.5–8.53 mM/L	82 MHz/mg ml^{-1}	0.05% of weight	Non-Intrusive	Label-Free	Not limited
[33]	0–700 mg/ml	3.13 e-02 MHz/mg ml^{-1}	-	Non-Intrusive	Label-Free	Not limited
[This work]	0–846.73 mg/ml (at THz) 0–500 mg/ml (at Microwave)	13.5 MHz/mg ml^{-1} (at THz) 12.77 e-2 MHz/mg ml^{-1} (at Microwave)	22.2 mg/ml (at THz) 73.3 mg/ml (at Microwave)	Non-Intrusive	Label-Free	Not limited

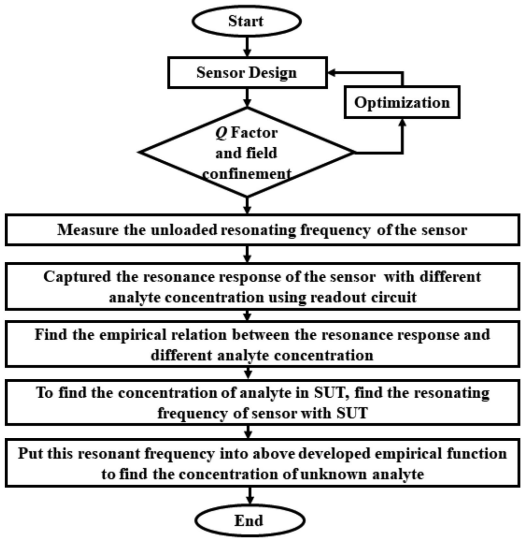

Fig. 16. Flowchart of proposed work and for determining unknown concentration of the analyte using proposed sensor.

The SUT has been infused through an inlet port with an optimum volume of 100 μL, and waste has been collected through an outlet port. A Keysight vector network analyzer (VNA) N9918A with an IF bandwidth of 100 Hz and an input power of -10 dBm is employed to acquired $|S_{11}|$ over a frequency span of 0.1-10 GHz with 1001 data points. The VNA is calibrated using the short-open-load-through (SOLT) method. All the sensing experiments were performed in a controlled environment of 25$\pm$1 °C.

The $|S_{11}|$ responses for different SUT have been captured and plotted in Fig. 14(b). The resonance frequency (f_r) increases from 3.20 GHz to 3.275 GHz by increasing the glucose concentration (χ) of the SUT from 50 mg/ml to 500 mg/ml. Fig. 14(c) plots the resonant frequency, $f_{r,}$ as a function of the χ. The proposed sensor provides a measured sensitivity, $S = 1.2771$e-4 MHz/mgml^{-1} at microwave frequency. An observation window has been set in the VNA from $F_{Smin} = 0.1$ GHz to $F_{Smax} = 10$ GHz with $n_p = 1001$ observation points, and thus it is set for a frequency resolution of 9 MHz. The *LOD*, i.e., resolution of the proposed sensor, is found to be 73.3 mg/ml at microwave frequency. The measurement uncertainty of the reflection response of the Keysight Fieldfox VNA N9918A is $\pm$ 0.006 dB, as described in the datasheet [27]. The sensor response has been taken in terms of the frequency change of the $|S_{11}|$ response. Measurement for each concentration of the analyte has been taken five times, and the measurement repeatability error of the sensor is found to be within $\pm$1 MHz. Further, corresponding performance parameters have been provided in Table III.

V. PROPOSED CUSTOMIZED READOUT CIRCUITRY

VNA is a widespread tool for the high frequency characterization. For characterizing one port device, VNA basically acts as a reflectometer. However, it is expensive and has a bulky benchtop setup, which limits its usage in many point of care (PoC) applications where portable and cost-effective system with lesser energy consumption is needed. In such cases, a low-cost customized arrangement to gauge the reflection can be used as a potential solution for the above-mentioned requirement. From Fig. 14(b), it is observed that due to resonant frequency shift, there is an amplitude difference in the S-parameter responses around at 3.225 GHz frequency for different concentrations of the SUTs. By capturing this amplitude around this frequency for different concentrations, one can develop PoC system for the proposed sensor. The customized read-out circuitry consists of a frequency synthesizer, coupler, and a power detector unit, as shown in Fig. 15(a). Fig. 15 (b) depicts the real-time read-out experimental system setup for the proposed sensor to be used for point of care applications. To provide a proof of concept, a signal generator has been used as an RF source that can be replaced by voltage controlled oscillator (VCO) chip later. A bi-directional coupler from Ametry part number CP20008A has been used here to capture the reflected microwave signal. This reflected microwave signal is fed to the AD8318 from analog devices, which acts

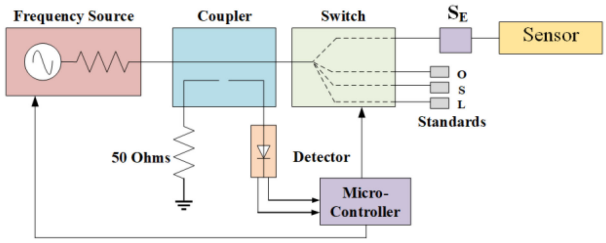

Fig. 17. Sensing system with self-calibrating functionality.

a power sensor with a gain unit and convert reflected power into voltage. This voltage has been measured using a digital oscilloscope. The output for the different concentrations of the SUTs has been captured using the proposed read-out circuitry and provided in Table IV. This analog DC voltage unit can be directly given to the data acquisition system for further signal processing and displaying the output. The step-by-step procedure to determine the unknown concentration of the analyte is also given in the flowchart, as shown in Fig. 16. Further, the comparison of the proposed sensor with state of the art has been given in Table V, which clearly signifies the potential of the proposed sensor for PoC detection of an analyte in biological samples.

VI. Conclusions & Future Scope

In the presented article, a highly sensitive, non-intrusive, label-free THz biosensor with microfluidic approach is proposed that can detect the concentration of glucose in an aqueous medium. An LSSP ring resonator, which confines and localizes the EM field, is used as a sensor. Due to this, the interaction of the EM wave with SUT increases and results in high sensitivity. The proposed sensor has a *High*–Q factor of *192*. A detailed theoretical analysis has been done for the proposed sensor, along with the numerical simulations. Due to the non-availability of the fabrication and characterization facilities at THz frequency, a proof of concept has been provided at microwave frequency. A customized read-out circuitry has been employed to use the proposed sensor as a PoC application. This sensor is an attractive choice for bio-logical applications and opens a new avenue to develop the lab-on-chip sensor.

All the sensing experiments were performed in a consistent, controlled environment of 25±1°C to reduce the environmental impact on the collected S-parameter data. However, to employ the proposed sensor in a more practical environment requires system having a low-cost read-out circuitry with easy calibration against the different environmental conditions such as temperature, humidity, pressure etc. and for the systematic error involved in the system. To compensate these effects on the sensor performance, a differential configuration approach can be used as discussed in [34] utilizing the proposed sensor. To eliminate the systematic error, a one-port easy self-calibration approach can be employed as shown in Fig. 17. In this approach, the customized read-out circuitry is connected to both the sensor as well as calibration standards using an SPQT (single pole quad through) switch. This switch can be digitally controlled for taking measurements and for performing calibration. The one-port calibration is based on the comparison of three measured calibration standards (open, short, and line) with their known reference values of reflection coefficient and find out the scattering error matrix, S_E. Once the elements values of scattering error matrix, S_E, have been found out the true values of the reflection coefficient of the SUT (Γ_{SUT}) can be determined from the measured reflection coefficient (Γ_{M}) according to [35] and given below in (18):

$$\Gamma_{SUT} = \frac{\Gamma_M - e_{00}}{\Gamma_M e_{11} - \Delta_e}, \text{where } \Delta_e = e_{00}e_{11} - (e_{10}e_{01}) \quad (18)$$

Where e_{00}, e_{01}, e_{10}, e_{11} are the error coefficients of matrix S_E.

Acknowledgement

The authors would like to thank Professor Arup Kumar Das, Department of Mechanical & Industrial Engineering, I.I.T. Roorkee and Professor Debabrata Sircar, Department of Biotechnology, I.I.T. Roorkee for their help in microfluidic channel fabrication and sample preparation.

References

[1] E. O. Blair and D. K. Corrigan, "A review of micro-fabricated electrochemical biosensors for DNA detection," *Biosens. Bioelectron.*, vol. 134, pp. 57–67, Jun. 2019.
[2] C. Chen and J. Wang, "Optical biosensors: An exhaustive and comprehensive review," *Analyst*, vol. 145, pp. 1605–1628, 2020.
[3] M. Zhang and J. T. W. Yeow, "Nanotechnology-based terahertz biological sensing: A review of its current state and things to come," *IEEE Nanotechnol. Mag.*, vol. 10, no. 3, pp. 30–38, Sep. 2016.
[4] P. H. Siegel, "Terahertz technology in biology and medicine," *IEEE Trans. Microw. Theory Technol.*, vol. 52, no. 10, pp. 2438–2447, 2004.
[5] D. Mittleman, *Sensing With Terahertz Radiation*, New York, NY, USA: Springer-Verlag, 2013.
[6] D. Jahn, A. Soltani, J. C. Balzer, M. Koch, and W. Withayachumnankul, "Fabry-Perot interferometer for sensing polar liquids at terahertz frequencies," *J. Appl. Phys.*, vol. 121, p. 204502, 2017.
[7] S. J. Park *et al.*, "Detection of microorganisms using terahertz metamaterials," *Sci. Rep.*, vol. 4, 2014, Art. no. 4988.
[8] M. Chen, L. Singh, N. Xu, R. Singh, W. Zhang, and L. Xie, "Terahertz sensing of highly absorptive water-methanol mixtures with multiple resonances in metamaterials," *Opt. Express*, vol. 25, no. 13, pp. 14089–14097, 2017.
[9] S. A. Maier, *Plasmonics: Fundamentals and Applications*, New York, NY, USA: Springer-Verlag, 2007.
[10] J. B. Pendry, L. Martín-Moreno, and F. J. Garcia-Vidal, "Mimicking surface plasmons with structured surfaces," *Science*, vol. 305, no. 5685, pp. 847–848, Aug. 2004.
[11] F. J. Garcia-Vidal, L. Martin-Moreno, and J. B. Pendry, "Surfaces with holes in them: New plasmonic metamaterials," *J. Opt. A: Pure Appl. Opt.*, vol. 7, pp. 97–101, 2005.
[12] A. P. Hibbins, B. R. Evans, and J. R. Sambles, "Experimental verification of designer surface plasmons," *Science*, vol. 308, no. 5722, pp. 670–672, 2005.
[13] W. Zhang, G. Zhu, L. Sun, and F. Lin, "Trapping of surface plasmon wave through gradient corrugated strip with under layer ground and manipulating its propagation," *J. Appl. Phys.*, vol. 106, no. 2, 2015.
[14] P. A. Huidobro *et al.*, "Magnetic localized surface plasmons," *Phys. Rev.*, vol. 4, 2014, Art. no. 021003.
[15] X.-L. Tang, Q. Zhang, S. Hu, A. Kandwal, T. Guo, and Y. Chen, "Capacitor-loaded spoof surface plasmon for flexible dispersion control and high-selectivity filtering," *IEEE Microw. Wireless Compon. Lett.*, vol. 27, no. 9, pp. 806–808, Sep. 2017.
[16] A. Kianinejad, Z. N. Chen, L. Zhang, W. Liu, and C.-W. Qiu, "Spoof plasmon-based slow-wave excitation of dielectric resonator antennas," *IEEE Trans. Antennas Propag.*, vol. 64, no. 6, pp. 2094–2099, Jun. 2016.

[17] N. Pandit, R. K. Jaiswal, and N. P. Pathak, "Plasmonic metamaterial-based label-free microfluidic microwave sensor for aqueous biological applications," *IEEE Sensors J*, vol. 20, no. 18, pp. 10582–10590, Sep. 2020.
[18] R. K. Jaiswal, N. Pandit, and N. P. Pathak, "Plasmonic metamaterial-based RF-THz integrated circuits: Design and analysis," *Nanoelectronics, Elsvier*, 2018, pp. 317–352.
[19] R. Zhang *et al.*, "Terahertz microfluidic metamaterial biosensor for sensitive detection of small-volume liquid samples," *IEEE Trans. THz Sci. Technol.*, vol. 9, no. 2, pp. 209–214, Mar. 2019.
[20] F. Cairone *et al.*, "3D-Printed micro-optofluidic device for chemical fluids and cells detection" *Biomed. Microdevices*, vol. 22, no. 37, 2020.
[21] S. Gagliano, G. Stella, and M. Bucolo, "Real-time detection of slug velocity in microchannels," *Micromachines*, vol. 11, no. 3, 2020.
[22] K. S. Cole and R. H. Cole, "Dispersion and absorption in dielectrics i. alternating current characteristics," *J. Chem. Phy.*, vol. 9, no. 4, pp. 341–351, 1941.
[23] A. H. Sihvola, "Mixing rules with complex dielectric coefficients," *Subsurface Sens. Technol. Appl.*, vol. 1, no. 4, pp. 393–415, 2000.
[24] Q. Tang *et al.*, "Microfluidic devices for terahertz spectroscopy of live cells toward lab-on-a-chip applications," *Sensors*, vol. 16, no. 476, 2016.
[25] M. M. Nazarov, O. P. Cherkasova, and A. P. Shkurinov, "Study of the dielectric function of aqueous solutions of glucose and albumin by THz time-domain spectroscopy," *Quantum Electron.*, vol. 46, no. 6, pp. 488–495, 2016.
[26] P. S. Nunes, N. A. Mortensen, J. P. Kutter, and K. B. Mogensen, "Refractive index sensor based on a 1D photonic crystal in a microfluidic channel," *Sensors*, vol. 10, no. 3, pp. 2348–2358, Mar. 2010.
[27] Keysight Fieldfox network analyzer data sheet, [Online]. Available: https://www.keysight.com/tw/zh/assets/7018-03314/data-sheets/5990-9783.pdf
[28] S. S. Ghoreishizadeh, C. Baj-Rossi, A. Cavallini, S. Carrara, and G. De Micheli, "An integrated control and readout circuit for implantable multi-target electrochemical biosensing," *IEEE Trans. Biomed. Circuits Syst.*, vol. 8, no. 6, pp. 891–898, Dec. 2014.
[29] K. A. Al Mamun, S. K. Islam, D. K. Hensley, and N. McFarlane, "A glucose biosensor using CMOS potentiostat and vertically aligned carbon nanofibers," *IEEE Trans. Biomed. Circuits Syst.*, vol. 10, no. 4, pp. 807–816, 2016.
[30] S. S. Ghoreishizadeh, I. Taurino, G. De Micheli, S. Carrara, and P. Georgiou, "A differential electrochemical readout ASIC with heterogeneous integration of bio-nano sensors for amperometric sensing," *IEEE Trans. Biomed. Circuits Syst.*, vol. 11, no. 5, pp. 1148–1159, 2017.
[31] A. E. Omer *et al.*, "Non-invasive real-time monitoring of glucose level using novel microwave biosensor based on triple-pole CSRR," *IEEE Trans. Biomed. Circuits Syst.*, vol. 14, no. 6, pp. 1407–1420, Dec. 2020.
[32] A. Kandwal *et al.*, "Highly sensitive closed loop enclosed split ring biosensor with high field confinement for aqueous and blood-glucose measurements," *Sci. Rep.*, vol. 10, 2020, Art. no. 4081.
[33] A. K. Jha *et al.*, "Broadband wireless sensing system for non-invasive testing of biological samples," *IEEE J. Emerg. Sel. Top. Circuits Syst.*, vol. 8, no. 2, pp. 251–259, Jun. 2018.
[34] M. C. Jain, A. V. Nadaraja, B. M. Vizcaino, D. J. Roberts, and M. H. Zarifi, "Differential microwave resonator sensor reveals glucose-dependent growth profile of e. coli on solid agar," *IEEE Microw. Wireless Compon. Lett.*, vol. 30, no. 5, May 2020.
[35] A. Basu, *An Introduction to Microwave Measurements*, Boca Raton, FL, USA, CRC Press, Taylor & Francis Group, 2015.

Nidhi Pandit (Graduate Student Member, IEEE) is currently working toward the Ph.D. degree with the Indian Institute of Technology Roorkee, Roorkee, India. Her current research is focused on exploring RF to THz integrated circuits, systems and sensors for biomedical and industrial applications and next generation communication.

Rahul Kumar Jaiswal (Graduate Student Member) is currently working toward the Ph.D. degree with the Indian Institute of Technology Roorkee, Roorkee, India. His current research is focused on exploring RF to THz integrated circuits, systems and sensors.

Nagendra Prasad Pathak (Member, IEEE) is currently a Professor with the Department of Electronics and Communication Engineering, IIT Roorkee. He has been a member of the Technical Committee on THz Technology and Applications (TC-MTT-21) since 2019. His current research interests include RF-THz Integrated circuits and sensors.